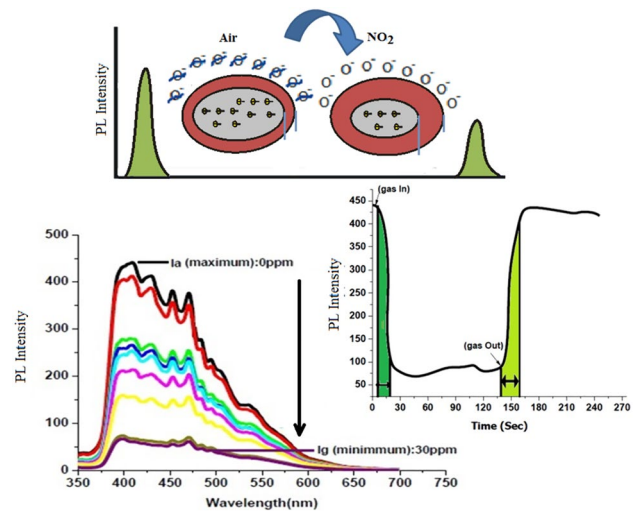RESEARCH ARTICLE

Room temperature optical gas sensing properties of Na- doped zinc oxide nanoparticles: improving response and recovery time

Neha Singh[1,2] · Jyoti Bamne[1] · Vivek Chandel[1] · Kajol Taiwade[1] · Abhinav Bhargav[1,3] · Nitu Singh[1] · Archana Nigrawal[1] · Fozia Z. Haque[1]

Abstract We report the results of NO_2 gas sensing performance of pure and Na doped (0.1%, 0.2%, and 0.3% w/w) zinc oxide nanoparticles synthesized via aqueous solution growth technique. The structural, morphological, and optical properties of the samples were characterized using X-ray diffraction (XRD), scanning electron microscopy (SEM), transmission electron microscopy (TEM), Raman spectroscopy, UV–Vis spectroscopy, and photoluminescence (PL) spectroscopy. PL and Raman spectral studies indicated that the ZnO nanoparticles possess more vacancies or lattice defects compared to the conventional ZnO nanoparticles (ZNP) prepared through various synthesis techniques. This work focuses on optical gas sensing at normal atmospheric pressure and room temperature to detect the presence of nitrogen dioxide gas. The optical NO_2 gas sensing studies revealed the substantial role of Na doping on the sensing properties of the synthesized samples, with gas concentrations ranging from 500 ppb to 30 ppm. Remarkably, 0.2% w/w Na-doped zinc oxide nanoparticles demonstrated an 84.7% response to 20 ppm NO_2 gas, with a quick response time (τ) of 9 s and a recovery time of approximately 20 s at room temperature and atmospheric pressure. The good sensing response, short response and recovery time, low detection limit and stability exhibited by 0.2% Na-ZnO nanoparticles make them promising candidates for fabricating efficient and reliable NO_2 sensors.

✉ Fozia Z. Haque
foziazia@rediffmail.com

[1] Optical Nanomaterials Lab, Department of Physics, Maulana Azad National Institute of Technology, Bhopal 462033, India

[2] Department of Physics, Banasthali Vidyapith, Tonk, Rajasthan 304022, India

[3] The Bhopal School of Social Sciences, Bhopal 462024, India

Graphical abstract

Introduction

In the modern era, we have established robust industrial infrastructure across a plethora of core industries including metals, chemicals, petroleum, food pesticides, plastics, detergents, fuels, paints, fertilizers solvents, edible food additives. However, these industries generate substantial industrial effluents and emissions, particularly toxic gases that are released into the atmosphere. Mining activities exacerbate this problem, primarily in the form of solid waste. Nitrogen dioxide is a significant contributor to atmospheric pollution and poses serious health risks. It absorbs visible solar radiation, reducing atmospheric visibility and has the

potential to influence global climate change if its concentration levels are elevated. NO_2, along with nitric oxide (NO), plays a critical role in the oxidizing capacity of the free troposphere, affecting air quality and public health. High NO_2 concentrations increase susceptibility to bacterial infections and lung cancer [1, 2]. Thus, developing a fast and effective NO_2 sensor that operates at room temperature is essential for immediate and accurate gas detection.

Currently available NO_2 sensors operate at relatively high temperatures (150–800 °C) and exhibit low sensing response (2–30%) at higher concentrations [4]. Therefore, ongoing research aims to improve sensor response and reduce operating temperatures by integrating catalysts, dopants or 2D materials [3]. In this context, our study investigates sodium-doped ZnO nanoparticles as a luminescence-based gas sensor for detecting NO_2 at room temperature with enhanced and rapid response.

Semiconductor nanostructures are extensively studied for their potential in chemical and biological sensors [4]. Metal oxide semiconductors, such as ZnO, are key components in sensor technology due to their chemical stability, low cost, and low power consumption [5]. ZnO nanoparticles, characterized by their atomic plane arrangement and surface defects, have shown as promising active materials for gas sensors [6–10]. High defect densities on nanoparticles increase the surface area for gas adsorption. Additionally, physical defects on nanomaterials can alter optical characteristics, leading to defect emissions often induced by oxygen vacancies, oxygen interstitials, zinc vacancies and zinc interstitials in the visible region [11]. Oxygen vacancies in the ZnO nanomaterials enhance the adsorption of negative ionic radicals such as O^- and O^{2-}, on the sensing material's surface [12, 13]. This phenomenon induces variations in the optical properties of the active material, including decreased optical intensity and shifts in the optical spectra.

Among the conventional sensing principles and techniques for studying materials for gas sensing devices, the resistive method is considered as the preferred one. This well-established technique operates on the principle of resistance modification, attributed to the chemisorption of gas molecules on the sensing layer. However, there are some ambiguities in the resistive sensing. For example, similar response curves can be observed for different gases at different temperatures with a single sensing material. These challenges have inspired the exploration of advanced measuring principles and techniques. In present paper, we report on luminescence-based gas sensing as a superior technique for studying the gas sensing properties of materials [14–20]. With reference to the above discussed findings we aim to justify the use of luminescence properties of samples for optical sensors.

This study focuses on the experimental results of pure ZnO and Na doped ZnO nanoparticles with luminescence gas sensing properties. ZnO is a promising material for gas sensing, demonstrating enhanced sensing properties for NO_2 gas, along with reduced response and recovery times at room temperature.

Experimental methods

Synthesis of p-ZnO and sodium doped ZnO

To prepare the aforementioned nanoparticles, Zinc Nitrate Hexahydrate $[Zn(NO_3)_2.6H_2O]$ (0.2 M) and Sodium nitrate (both purchased from Sigma-Aldrich) were dissolved in 50 ml of deionized (DI) water with continuous stirring at room temperature for 5 min. NaOH was then added dropwise, producing $Zn(OH)_4$ ions in the solution throughout this procedure. After 10 min, a certain amount of (BTMAH) ionic liquid was added to the prepared solution with continuously stirring for 15 min at room temperature. ZnO precursors containing Na dopant were prepared with 0.0, 0.1, 0.2 and 0.3% w/w of sodium nitrate and, the prepared solution was kept in a temperature-controlled oven at 95 °C for 4 h. The resultant white precipitate of undoped and sodium-doped ZnO was separated by centrifugation and washed multiple times with double distilled water. Finally, the crystalline ZnO powder was dried at 200°C for 4 h in the temperature-controlled oven.

Characterization

Powder X-ray diffraction (XRD) of the four samples were collected using a Bruker D8 Advance X-ray beam diffractometer with Cu K_α radiation working at 40 kV and 40 mA, equipped with a position sensitive detector (LynxEye) based on Bruker AXS compound silicon strip technology. Scans were performed from 20º to 80º of 2θ for each sample. The diffraction peaks of the crystalline phase were compared with those of the standard compound reported in the JCPDS data files No. PDF#790,206 ICSD#: 065120. Scanning electron microscopy (JEOL-JSM-6390), Energy dispersive X-ray (EDX) and Transmission Electron Microscopy (TEM) were used to define the morphology and elemental composition of the prepared samples. Brunauer, Emmett, and Teller (BET) surface analysis data were also collected for the synthesized samples using Autosorb (iQ). Fourier Transform Infrared (FTIR) spectroscopy (Bruker, Germany) was used to determine the chemical compositions at room temperature, with the Model-Vertex 70-spectroscopy in the 4000 to 300 cm^{-1} range. Raman spectroscopy data was collected using the Jobin Yvon Horibra Labram-HR visible spectrometer, covering a Raman shift range from 50 cm^{-1} to 4000 cm^{-1}. The optical properties of materials were determined using photoluminescence (PL) spectroscopy, with

data collected using fluorescence spectrophotometer (F-7000 Hitachi) excited with a Xenon lamp of wavelength 237 nm at room temperature. UV–Visible spectroscopy was performed using Perkin Elmer (Lambda 950) spectrophotometer.

Gas detection

For optical gas detecting and estimation, the samples were excited by a Xenon lamp light source (F-7000 Hitachi) at 237 nm excitation wavelength. The samples were placed on a quartz plate using a spin coater and set inside a quartz sample holder at room temperature. Details of the sample holder can be found in the patent description of a granted patent on a Sample Holder for Optical Gas Sensing by the investigator [45]. The patented sample holder (Fig. 1) was placed inside the spectrophotometer chamber for optical estimations, and then the chamber was filled with the required amount of NO_2 gas [21, 22]. The spectral response data were recorded before and after exposure of Nitrogen dioxide gas for comparison. The spectral responses of all pure ZnO and Na-doped ZnO samples were recorded for NO_2 gas at various concentrations (500 ppb to 30 ppm).

Results and discussions

XRD

The XRD patterns of the undoped and Na-doped ZnO powders are displayed in Fig. 2 The recorded data for all the samples was utilized to calculate the peak broadening and crystallite size. By comparing the patterns with the standard XRD patterns of ZnO samples (PDF#790,206 ICSD#: 065120), it is evident that all identified peaks correspond to the characteristic peaks of hexagonal wurtzite ZnO with space group *P63mc* [23]. The full width at half-maximum (FWHMs) for three significant diffraction peaks of the 0.1% Na-doped sample, ((100), (002), and (101)), were more than twice that of the undoped material. Furthermore, the FWHM of the Na-doped nanoparticles continued to increase as the Na doping concentration increased from 0.1 to 0.3%.

The crystallite sizes of the specimens were calculated using Scherrer's formula. The average crystallite diameter of ZnO nanoparticles doped with 0.1% Na were substantially reduced from 23.95 to 20.51 nm, as shown in Table 1. This decrease in crystallite diameter is attributed to the crystal lattice distortion caused by the incorporation of Na^+ dopant into the ZnO crystal. The distortion is induced by the significant difference in ionic radii between Zn^{+2} ($0.74°$ Å) and Na^+ ($0.89°$ Å.), as well as by the increase in FWHM intensity [23, 24]. Dislocation or lattice defects can be attributed to the microstrains. Dislocation density can be used to represent the dislocation in a crystal system. The equation used to calculate the dislocation density (δ) is shown below.

$$\delta = 1/D^2 \tag{1}$$

Variation in the lattice parameters (a and c) and the corresponding unit cell volume ($V = 0.866a^2c$) of the as-prepared samples were determined and are listed in Table 1. It is observed that with the increase in Na^+ ion concentration, the
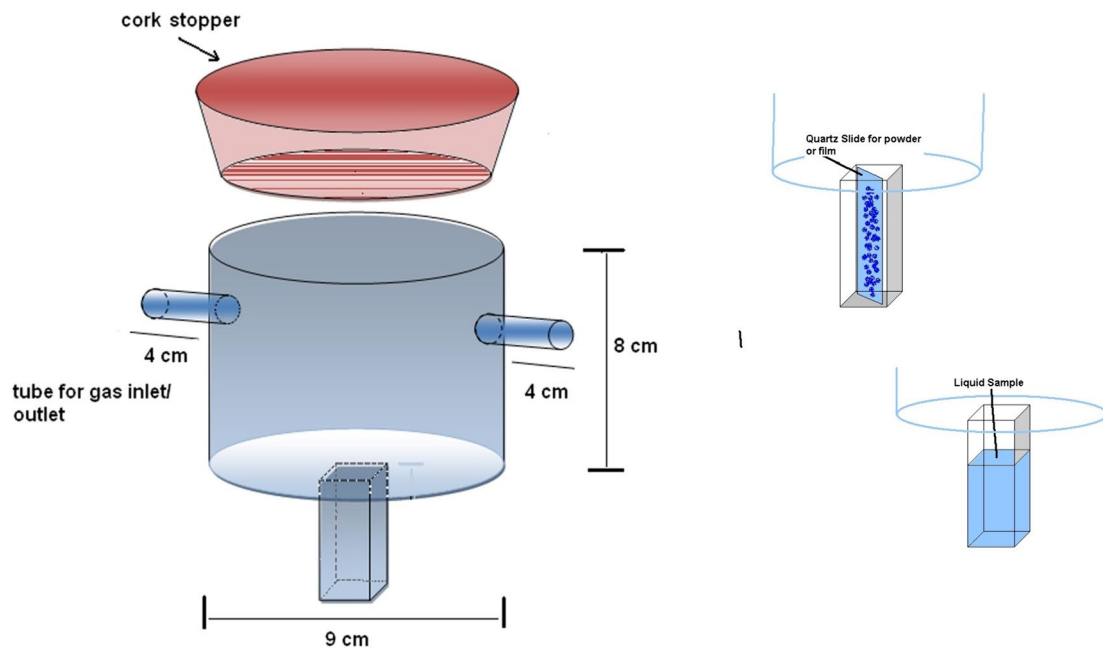

Fig. 1 Description of patented sample holder for Optical Gas Sensing

Fig. 2 XRD patterns of pure and Na-doped ZnO nano powders at various concentrations
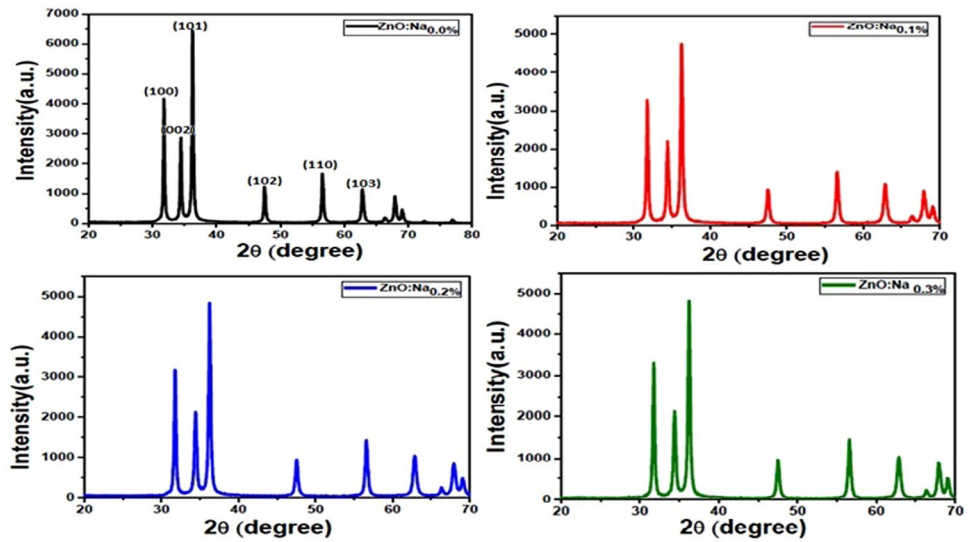

Table 1 Comparative analysis of crystallite size, microstrain and dislocation density of pure and Na doped ZnO nanoparticles

Concentration of sodium	Lattice parameters		Aspect Ratio (c/a)	Strain(Å)	Volume (Å)³	Dislocation Density 'δ' (× 1015 lines/m²)	Crystallite size 'D' (nm)
	a (nm)	c (nm)					
ZnO:Na$_{0.0\%}$	0.3259	0.5323	1.60	0.002744	48.96	1.74	23.95
ZnO:Na$_{0.1\%}$	0.32389	0.5289	1.632	0.003525	48.05661	2.44	20.23
ZnO:Na$_{0.2\%}$	0.32393	0.5289	1.632	0.003571	48.07437	2.57	19.7
ZnO:Na$_{0.3\%}$	0.32408	0.5291	1.632	0.003455	48.12236	2.93	18.45

cell volume of Na-substituted ZnO nanoparticles substantially increases, which is in accordance with the Vegard's law [46]. The standard value of c/a ratio for pristine ZnO nanoparticles is reported around ~ 1.6, and the c/a ratio for the synthesized Na-doped system has the value of 1.632, which is consistent with the reported value, it also suggests that the substitution of Na$^+$ takes place by producing some lattice defects but without affecting the overall cell structure of ZnO. From Table 1, it was reckoned that with the increase in Na$^+$ ion concentration, the diffraction peak tends to show broadening and marginal shift towards the lower Bragg angle (2θ), which represents the reduction in crystallite size as well as presence of uniform strain [46].

The degree of microstrain (ε_{zz}) was calculated and tabulated in Table 1 for all the samples along c axis, using the equation.

$$\varepsilon_{zz} = (c - c_0) * 100 / c_0 \tag{2}$$

where c_o is the unstrained lattice parameter and c is the lattice parameter computed from the XRD data [46]. The relation between crystallite size and strain is estimated by Williamson–Hall (W–H) method [46]:

$$\beta\cos\theta = k\lambda/d + 4\varepsilon\sin\theta \tag{3}$$

The above formula represents Uniform Deformation Model (UDM), which presumes that the strain is uniform in all crystallographic orientations [46].

Table 1 shows the calculated microstrain and dislocation values. With the increase in Na concentration from 0.1 to 0.3% in the as-prepared ZnO samples, the average crystallite size of ZnO:Na nanoparticles decreases very slightly, from 23.95 to 18.45 nm.

The data of crystallite size deduced from both Debye–Scherrer equation and W–H analysis are listed in Table 1. From Table 1, it is observed that the crystallite size of the Na-substituted ZnO nanoparticles reduces with increase in the Na$^+$ ion content. This observation is supported well by the corresponding increase in the value of strain (ε). Positive value of ε_{zz} is due to the tensile strain and is in good agreement with the calculated values from W–H analysis [12]. The crystallite size (d), computed using Scherrer's formula and W–H analysis, decreases with increase in Na$^+$ dopants entailing that Na$^+$ ions influences the nucleation and growth rate of nanocrystals. Singh et al. [46] reported that introduction of metallic-ion in an interstitial position alters the concentration of the interstitial Zn, O, and Zn vacancies, which in turn is reflected via changes in Bragg's angle (2θ), broadening of peak width (β), and reduction of crystallite size.

Morphology of pure and Na doped zinc oxide nanoparticles:

The surface structure of nanomaterial is crucial for all applications. The scanning electron microscope (SEM) and Transmission Electron Microscopy (TEM) images confirm the formation of nano-sized particles as shown in Figs. 3 and 4. The SEM images in Fig. 3 depict that the particles in the undoped ZnO were larger than those in the Na-doped samples. As the concentration of sodium dopant increased from 0.1 to 0.3%, it is clearly observed that particle dimensions remained in the nanometer range, with no significant change in morphology. The decrease in particle size is likely related to an increase in alkalinity, which inhibits grain growth. The increase in sodium concentration raises the pH of the precursor solution, facilitating the formation of nanoparticles.

A selected area electron diffraction (SAED) design was recorded under TEM under proper recording conditions as per its mandate. Several areas were examined before capturing the SAED pattern. In all the observed areas, only restricted rings were noticed. The SAED pattern of pure ZnO nanoparticles is shown in Fig. 4b. The diffused contrast over the Debye ring throughout the sample may result from the combined effect of many ZnO nanoparticle barriers. The SAED provides data on the orientation of crystallographic planes in a given location. The relative atomic compositions of pure ZnO nanoparticles were investigated through energy-dispersive X-ray spectroscopy (EDS) [25].

Brunauer, Emmett, and Teller (BET) surface area analysis

BET (Brunauer–Emmett–Teller) was used to calculate the surface area, and Barrett- Joyner- Halenda (BJH) were used to calculate the pore size and pore volume of synthesized samples. The value of surface area obtained for pure ZnO nanoparticles is 17.0832 m^2/g, which is lesser than that of Na-doped ZnO samples, as shown in Table 2. The increase in specific surface area at 0.3% doping concentration may be attributed to the decrease in grain size.

Raman analysis

The quality and crystal structure of pure and sodium doped zinc oxide nanoparticles were clarified using Raman scattering technique. Raman active modes are A_1, E_1 and $2E_2$ modes, while the Raman stationary mode is B_1. Furthermore, for a wide range of electrostatic forces, the A_1 and E_1 modes are polar and these modes may be further split into transverse optical (TO) and longitudinal optical (LO) phonons. The dominance of electrostatic forces in this region is due to the limited range of interatomic interactions, and anisotropy is observed with the TO-LO splitting being larger than the A_1–E_1 Splitting. Figure 5 shows the excitation at 533 nm using a He–Ne laser, with significant shifts in the Raman spectrum for pure and sodium doped zinc oxide nanoparticles. For second-order Raman spectrum ($2E_2^M$ and E_2), the peaks located at 332 cm^{-1} to

Fig. 3 SEM images of Na doped ZnO nanoparticles: **a** undoped, **b** 0.1%, **c** 0.2%, **d** 0.3%
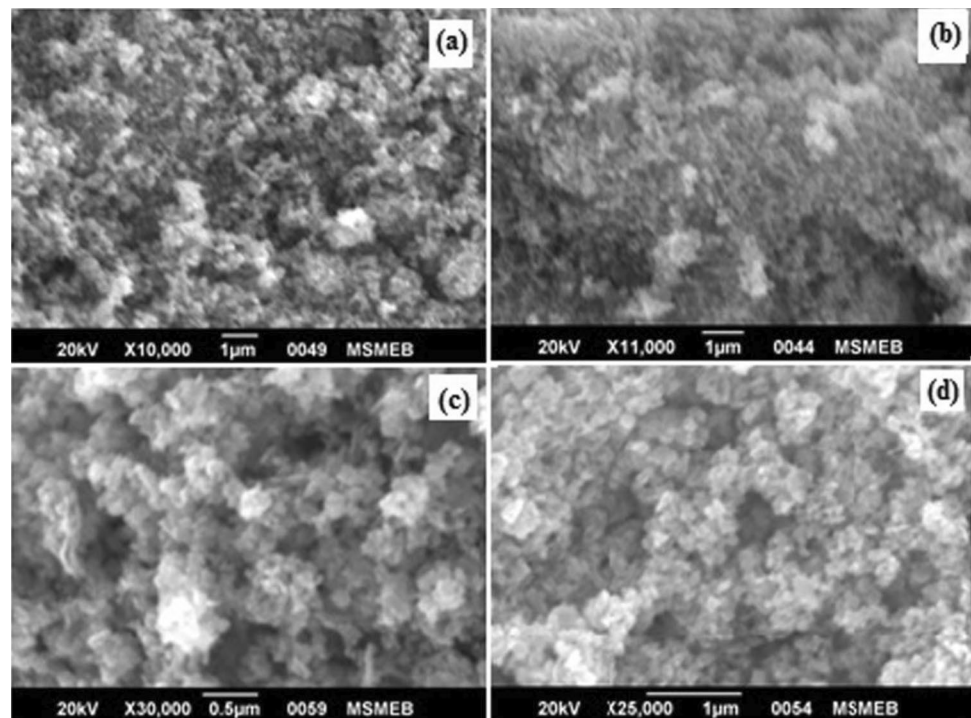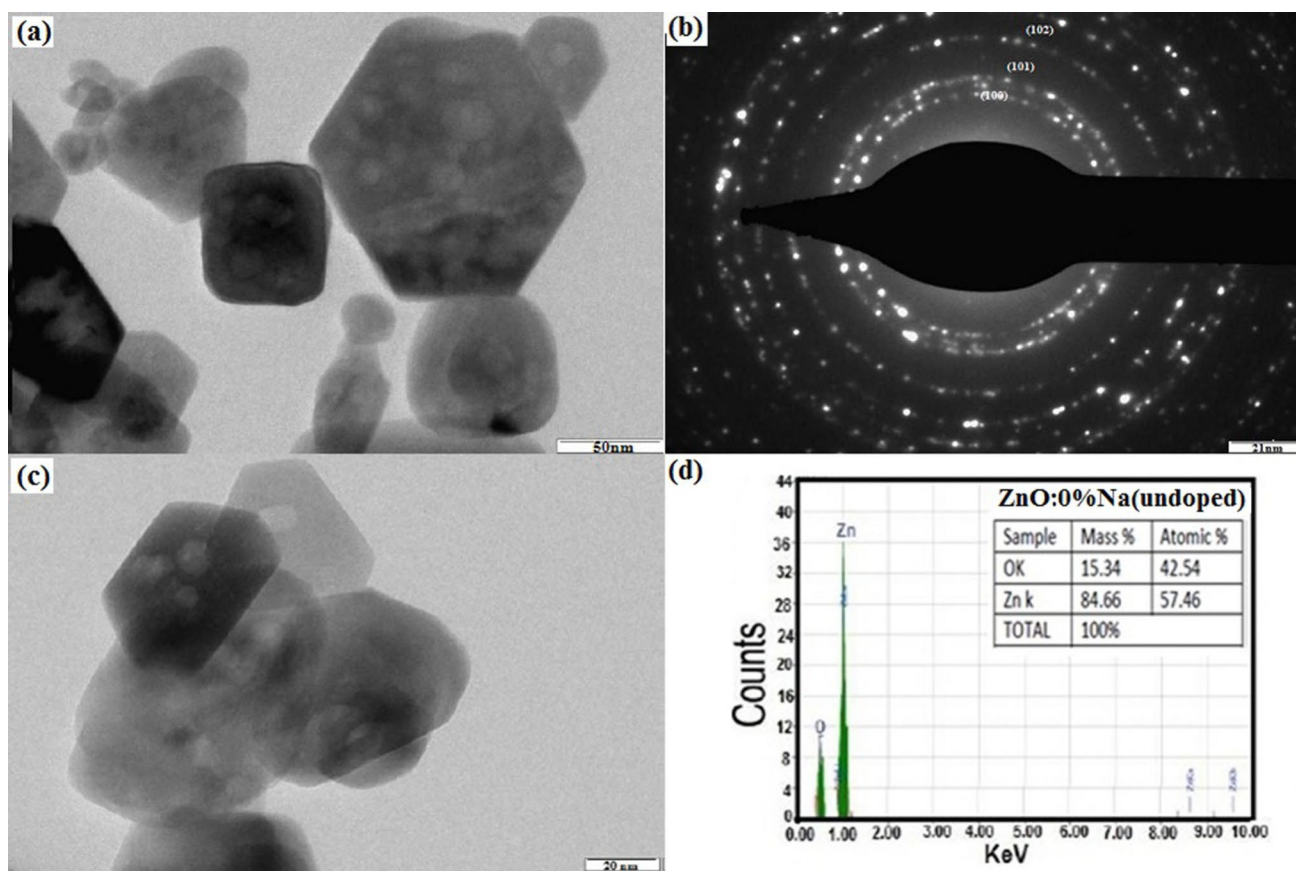
Fig. 4 **a** TEM image of pure, **b** Selected-area electron diffraction pattern of pure, **c** ZnO: $Na_{0.2\%}$ samples, **d** EDS spectra of pure ZnO samples

Table 2 BET surface area and BJH pore diameter of pure ZnO and sodium doped ZnO nanoparticles

Sample	BET surface area (m^2/g)	BHJ	
		pore volume (cc/g)	Pore size (nm)
ZnO	17.0832	0.0092427	1.6672
ZnO:$Na_{0.3\%}$	29.7019	0.550016	1.8064

331.34 cm^{-1} and 439.35 cm^{-1} to 438.05 cm^{-1} are assigned. The E_2 (high) mode of ZnO, observed for hexagonal phase centered at 439.35 cm^{-1} and 438.05 cm^{-1}, demonstrates that the ZnO:Na samples have the wurtzite structure [26–28]. The peak located at ~ 581.70 cm^{-1} to 581.73 cm^{-1} is recognized as the superimposition of polar modes A_1^L and E_1^L, while the E_1^L mode is due to the presence of oxygen vacancies and interstitial Zn ions. The frequency of 1LO phonon mode indicates the presence of ZnO according to the theory of polar optical phonons in wurtzite nanocrystals. A shift from higher wavenumber 581.41 cm^{-1} to 582.60 cm^{-1} for the 1LO phonon mode is also observed. Due to the sodium concentration, the intensity and broadness of peak increase. Because of the nanosized dimension of the samples, the
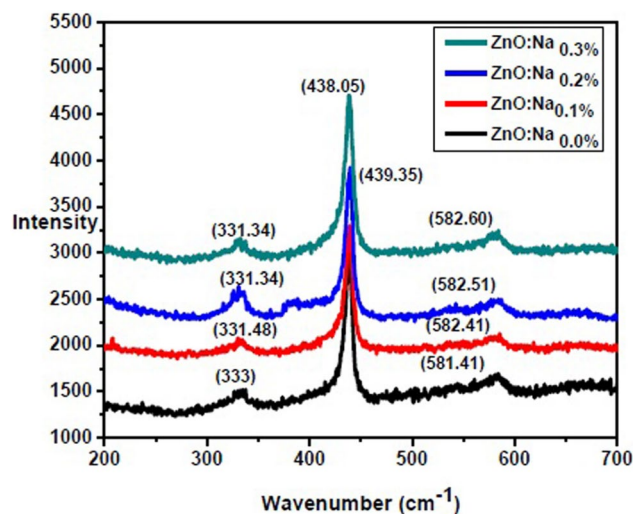

Fig. 5 Raman spectra of **a** undoped- ZnO, **b** ZnO: $Na_{0.1\%}$, **c** ZnO: $Na_{0.2\%}$ and **d** ZnO: $Na_{0.3\%}$ samples

central peak in these spectra is at somewhat lower frequencies than in bulk crystals. The structure of ZnO inferred from

Table 3 Functional groups present in ZnO samples at different concentration of Na

Functional group	Wavenumber cm^{-1}			
	ZnO:Na$_{0.0\%}$	ZnO:Na$_{0.1\%}$	ZnO: Na$_{0.2\%}$	ZnO:Na$_{0.3\%}$
O–H	1380.31	1380.31	1380.31	1380.31
Zn–O	465.46	560.88	419.56	577.11
C=O	2348.24	2359.12	2359.12	Not present
–OH	3445.58	3430.31	Not present	3445.58

the Raman analysis is also well correlated with the XRD results as discussed above.

FTIR analysis

FTIR spectroscopy was implemented to identify the chemical functional groups of the as-prepared samples, and the results are shown in Table 3. The particle size and morphology generally influence the chemical properties of the samples [29]. Figure 6 shows FTIR spectra of the prepared pure and Na-doped ZnO nanoparticles. In these samples, Zn–O bond is observed at 465.46 cm^{-1} for p-ZnO, 560.88 cm^{-1} for Na = 0.1%, 419.56 cm^{-1} for Na = 0.2%, and 577.11 cm^{-1} for Na = 03%. According to the well-known theories of vibrational modes in mixed crystals, the replacement should result in an upward shift of the crucial transverse optical phonon mode. Here, the Na atom is slightly lighter than Zn atom. C=O stretching bonds located at 2348.24 cm^{-1} for p-ZnO, and 2359.12 cm^{-1} for 0.1% and 0.2% Na-doped ZnO are attributed to asymmetric and symmetric C=O stretching vibration modes. The presence of C=O may be due to the atmospheric CO_2. The O–H absorption bands observed at 1380.31 cm^{-1} in all Na-doped ZnO samples are attributed to the bending of the hydroxyl group. The peaks located at 3445.58 cm^{-1} for pure ZnO and 3430.31 cm^{-1} for 0.1 and 0.3% Na-doped ZnO, likely indicate the presence of –OH residues due to atmospheric pressure [30, 31]. Table 3 presents the corresponding peak positions. The interplay and interactions between surface chemistry, ambient conditions, doping effects, and surface defects are the main factors responsible for the random appearances and disappearances of the OH and C-O bond in Na-doped ZnO system. Na doping in ZnO nanoparticles can influence surface sites or introduce defects in the synthesized system, these imperfections or sites facilitates the adsorption or desorption of molecules containing OH and C-O bond. Surface functional groups may arise or vanish arbitrarily, depending on the quantity and distribution of these sites throughout the sample's surface. The FTIR analysis confirms that the samples are devoid of any other organic contaminants, making them suitable for further research.
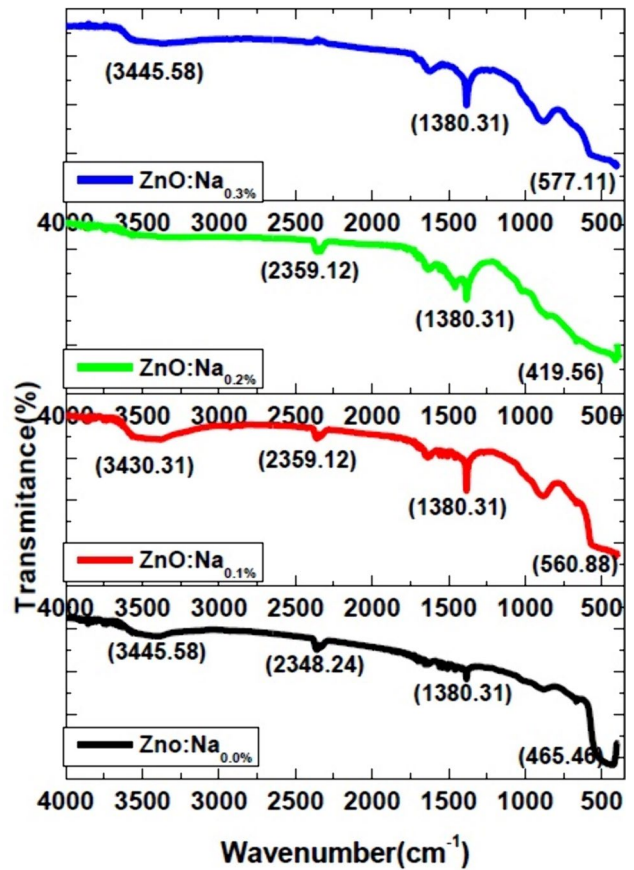

Fig. 6 FTIR spectra of undoped ZnO: Na$_{0.0\%}$, ZnO: Na$_{0.1\%}$, ZnO: Na$_{0.2\%}$, ZnO: Na$_{0.3\%}$ nanoparticles

UV–Visible analysis

The Tauc plot of pure and Na-doped ZnO nanoparticles as a function of eV is shown in Fig. 7. The optical band gap energy (E_g) of prepared samples was calculated using the following Tauc equation:

$$\alpha h\nu = A\,(h\nu - Eg)^n \tag{4}$$

where A is an energy-independent constant, E_g is the band gap energy, α is the absorption coefficient and n is a parameter that defines the possible optical transitions. In Eq. 4, n = 3 refers to the indirect forbidden transition, n = 2 an indirect allowed transition, and n = 1/2 a direct allowed transition. Figure 7 shows the Tauc plot of band gap energies of the prepared samples at various concentrations of sodium doping [32]. In accordance with the reported results, the band gap energy of pure ZnO was found to be ~ 3.03 eV [32]. Table 4 shows the increase in band gap energy from 3.03 eV (ZnO: Na$_{0.0\%}$) to 3.08 eV (ZnO: Na$_{0.3\%}$) with the increase in concentration of Na.

Fig. 7 Tauc plot of $[F(R).h\nu]^2$ versus photon energy hν for p-ZnO and sodium (0.1, 0.2 and 0.3%) doped ZnO specimens
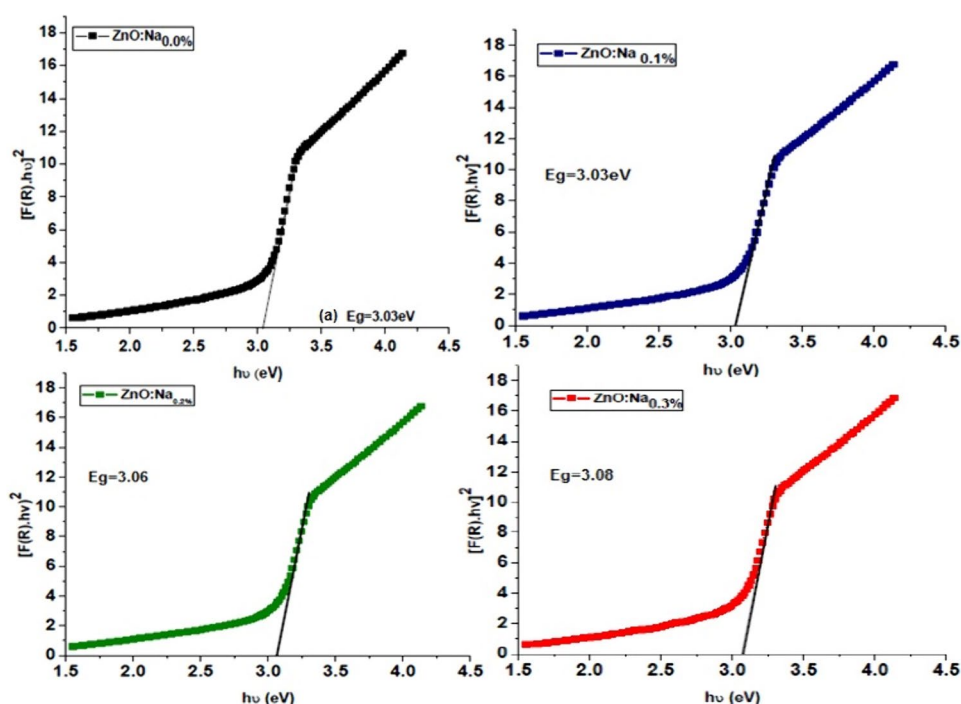

Table 4 Band gap and spectral band positions obtained from UV–Vis and PL emission spectra

Samples	Band gap energy E_g, eV	Band positions in nm from PL emission spectra $\lambda_{ex} = 237$ nm
ZnO:Na$_{0.0\%}$	3.03	348, 452, 471, 538
ZnO:Na$_{0.1\%}$	3.03	409, 430, 452, 470, 538
ZnO:Na$_{0.2\%}$	3.06	396, 410, 430, 453, 469, 538
ZnO:Na$_{0.3\%}$	3.08	396, 410, 430, 453, 469, 540

It can be estimated from the absorbance spectrum (Fig. 7), that the absorption spectra show a blue shift in the absorption edge of the Na-doped ZnO samples with increase in Na$^+$ ion content and also in contrast to undoped ZnO sample. The shape and width of the absorbance peak presents a general idea about the particle size distribution in the synthesized system [46]. According to Kubo theory [32, 46], the shift of absorption band to the blue region of visible spectrum with decrement in particle size results in the increase in band gap. It has also been reported in the previous findings [15, 32, 46] that, for nano-scaled particles, the separation of energy level occurs, as of when the interaction between the atomic energy levels is reduced and quantum effects are dominant. The optical band gap energy of the samples was deduced by extrapolating the linear portion of the graph on y axis [46].

From Fig. 7 and Table 4, it can be observed that, with increase in the Na$^+$ ion content, the samples denote a blue shift in the absorption edge which indicates the reduction in particle size and increase in the energy band gap. This is

concluded in accordance with the Kubo's theory [46] and the results obtained are confirmed with the TEM analysis.

The observed discrepancy in the optical band gap may be attributed to the variations in the stoichiometry of ZnO samples and the concentration of the associated point defects. This range of variation in bandgap energy supports the material's potential to match the energy levels of oxidizing or reducing gases, facilitating a higher rate of electron exchange and thereby improving the gas response.

Photoluminescence spectroscopy

Photoluminescence (PL) emission spectra of pure and Na-doped ZnO samples, excited at an excitation wavelength of 237 nm at room temperature, are shown in Fig. 8. Table 4 shows the characteristics wavelength (nm) of various peaks of the samples (Figs. 9a, b, c and d).

In the PL spectra (Fig. 8), the UV band shows a very weak peak at 348 nm for the p-ZnO sample, which disappears with sodium doping (0.1, 0.2 and 0.3%). This disappearance may be attributed to the quantum confinement effect and recombination of free excitons. Across all spectra, from p-ZnO to 0.3% Na-doped ZnO, a broad and high-intensity visible emission is observed. Green emission peaks, appearing as humps, were observed in all samples around 538 nm, 540 nm and 538 nm, which are caused by singly ionized oxygen vacancies and recombination of electrons with singly ionized O$^-$ vacancies in ZnO. This effect is further influenced by the quantum confinement effect due
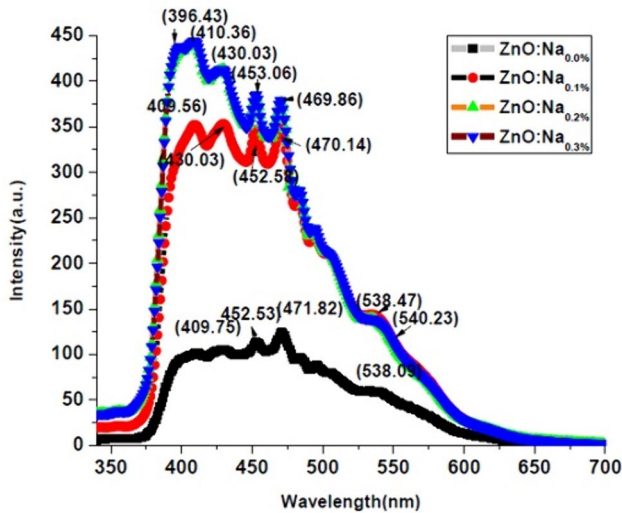
Fig. 8 Room temperature photoluminescence spectrum of pure and sodium doped zinc oxide particles at an excitation wavelength of 237 nm

to structural modifications of ZnO samples with varying Na concentration [33].

Due to the surface defects and confined particle size in ZnO samples, blue emissions were observed at 452 nm, and 471 nm in p-ZnO, 452 nm and 470 nm in 0.1% Na-doped ZnO, at 453 nm and 469 nm in 0.2% and 0.3% Na-doped ZnO respectively. These are in good agreement with previously published reports [34, 35]. The violet emission peak is formed by the recombination of electrons at zinc interstitials (Zn_i) with holes in the valance band at 409 nm, 409 nm, 396 nm and 410 nm [34].

It is notable that the blue emission is significantly high in pure ZnO, but gradually decreases relative to the violet emission with increasing Na-doping levels [47]. Additionally, the green emission becomes more pronounced due to the increase of singly ionized oxygen vacancies with the increased concentration of Na^+ ions.

When comparing undoped ZnO sample with Na-doped ZnO samples, it is evident that the violet emission intensity increases due to enhanced recombination of electrons at zinc interstitials (Zn_i) and holes in the valance band. The blue and green emissions, attributed to zinc and oxygen vacancies respectively, are also affected. It confirms that Na-doped samples exhibit strong violet luminescence compared to p-ZnO. While many studies have focused on blue-emission in the luminescence spectra of semiconductor nanocrystals, few have addressed nano-sized sodium doped luminous materials.

The luminescence mechanism in the semiconductors involves the recombination of electrons in the conduction band with holes in the valence band. Quantum confinement typically requires a larger band gap to induce blue-emission

in luminescence. However, in Na-doped ZnO, the luminescence is caused by transitions between energy levels of Na^+ atoms serving as the luminescence centers. This necessitates a new interpretation to explain the blue-emission in the luminescence spectra of Na-ZnO nanoparticles. Additionally, nanometer-sized particles significantly increase surface energy, altering the crystal field around the immediate environment of Na^+. These factors result in intensified violet-blue emission in $ZnO:Na^+$ and reduced particle size with 0.1% to 0.3% Na-doping. This finding is consistent with UV–Vis and XRD analysis. The gradual occurrence of peaks in the visible region suggests that these materials are promising candidates for optical sensing device.

Gas sensing studies

Optical sensing

The operational principle of metal oxide sensors is based on the adsorption and desorption of gas on the sensor surface, which leads to changes in the optical properties or PL intensity of these nanomaterials [36]. When the gas molecules interact with the n-type semiconductor material, they adsorb onto the surface and capture electrons from the material, resulting in a measurable change in its optical properties.

In the present study, the surface of ZnO directly adsorbs NO_2 gas according to the following reaction:

$$NO_{2(gas)} + e^- \rightarrow NO_{2(ads)} \tag{5}$$

Furthermore, NO_2 adsorbed on the surface of ZnO decomposes, into nitrogen monoxide (NO) molecule and an oxygen atom, which are then adsorbed onto the surface of ZnO:

$$NO_{2(gas)} + e^- \rightarrow NO_{(gas)} + O^-_{(ads)} \tag{6}$$
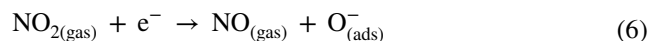
Subsequently, NO molecules may adsorb onto the surface of ZnO. NO molecules can also be directly adsorbed or dissociated using the methods described below:

$$NO_{(gas)} + e^- \rightarrow NO_{(ads)} \tag{7}$$

$$NO_{(gas)} + e^- \rightarrow N_{(gas)} + O_{(ads)} \tag{8}$$

Due to these reactions, electrons of ZnO are captured by the adsorbed species, leading to the formation of a depletion layer onto the ZnO surface. This depletion layer reduces the number of free electrons available for radiative recombination, which is reflected in the observed decrease in photoluminescence (PL) intensity in the presence of NO_2. Therefore, the reduction in PL intensity under NO_2 exposure is attributed to the electron capture and the formation of the depletion layer.
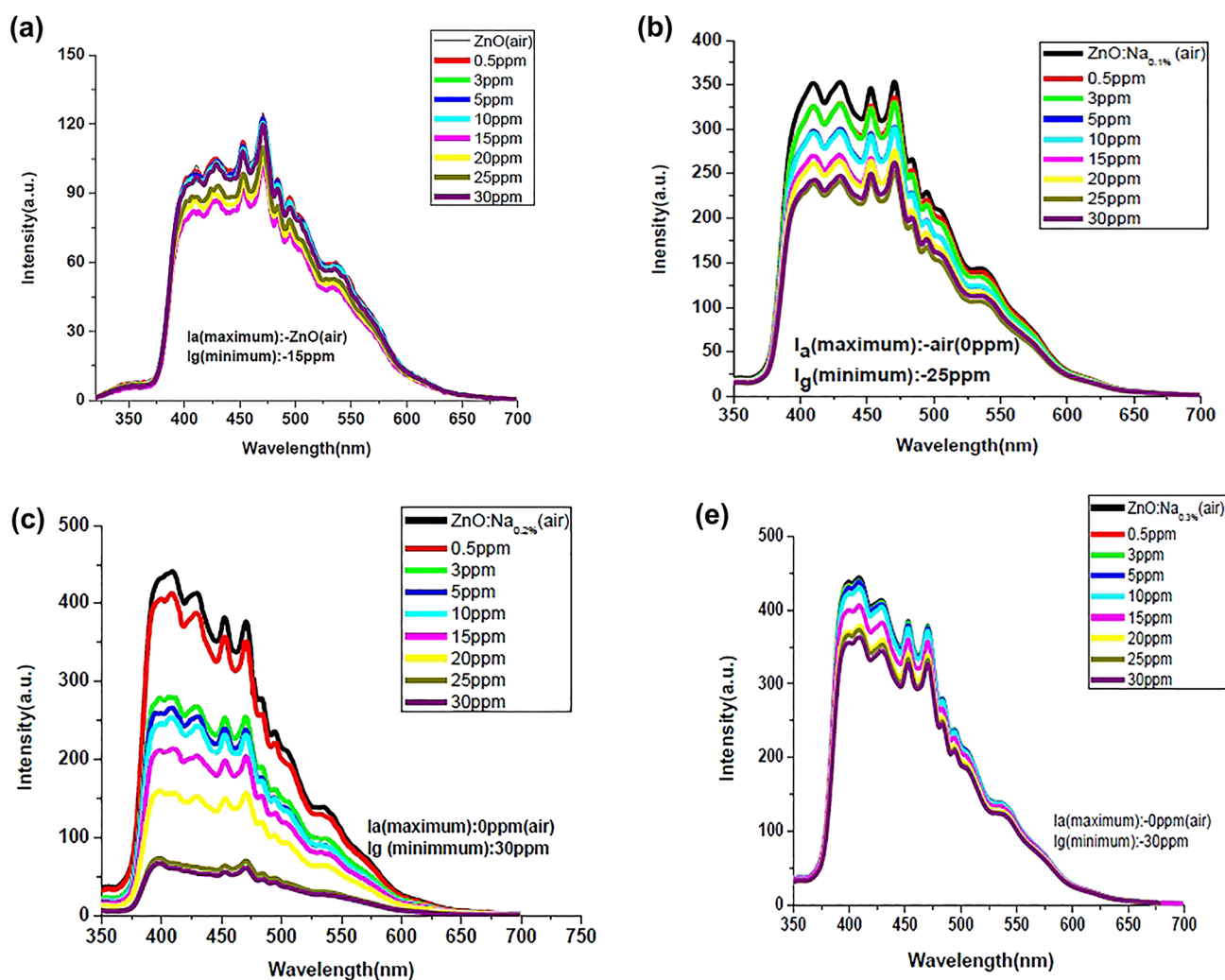
Fig. 9 a Room temperature Photoluminescence Spectra of pure ZnO at different concentrations of NO_2 (500 ppb to 30 ppm). **b** Room temperature Photoluminescence Spectra of ZnO:$Na_{0.1\%}$ at different concentrations of NO_2 (500 ppb to 30 ppm). **c** Room temperature Photoluminescence Spectra of ZnO:Na $_{0.2\%}$ at different concentrations of NO_2 (500 ppb to 30 ppm). **d** Room temperature Photoluminescence Spectra of ZnO:$Na_{0.3\%}$ at various concentrations of NO_2 (500 ppb to 30 ppm)

Figure 9a, b, c and d presents the PL spectra of pure and Na-doped ZnO samples at room temperature, excited at 237 nm in the presence of NO_2 gas at various concentrations (500 ppb to 30 ppm). The hexagonal lattice structure of ZnO, where Zn atoms occupy half of the tetrahedral sites and all the octahedral sites, provides a relatively open framework that accommodates both inherent defects and extrinsic dopants. The Substitution of Zn^{2+} with Na^+ ions introduces additional defects and oxygen vacancies in the ZnO crystal lattice. Consequently, Na-doped ZnO exhibits a higher concentration of oxygen vacancies compared to pristine ZnO. These oxygen vacancies create extra adsorption sites for NO_2 molecules, thereby enhancing the surface reactivity and, in turn, improving the sensing characteristics.

Figure 9 also illustrates the overlapping PL spectra of ZnO and Na-doped ZnO across a NO_2 concentration range from zero ppm to 30 ppm. Upon exposure to NO_2 gas, a significant decrease in PL intensity is observed, while no noticeable shift in the emission peak position or change in its line shape is detected. This decrease in PL intensity can be attributed to the interaction between NO_2 molecules and ZnO, which involves the adsorption of NO_2 molecules that capture electrons from the ZnO material [37]. When NO_2 molecule interacts with pure and Na doped ZnO, it can be adsorbed by capturing an electron from the material in multiple ways. Specifically, the adsorption of NO_2 leads to the formation of a depletion layer on the ZnO surface, resulting in a reduction of free charge carriers and an increase in non-radiative recombination processes. This phenomenon explains the observed decrease in PL intensity under NO_2 exposure compared to the initial value when the material is exposed to air. If the adsorption processes are reversible,
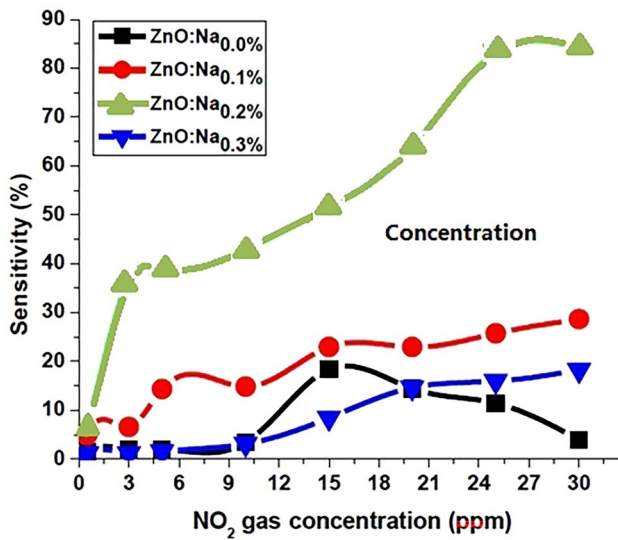
Fig. 10 Sensor response of pure ZnO sample with all the Na-ZnO specimens for different gas concentrations from 500 ppb to 30 ppm
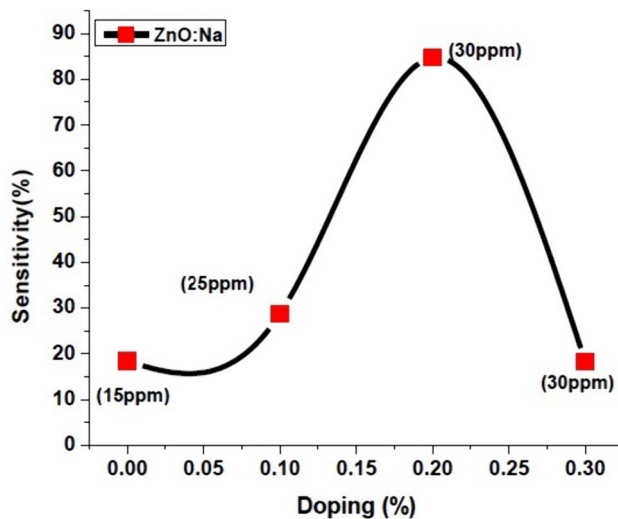

Fig. 11 Highest Response of pure and Na doped ZnO for highest concentration of NO_2 gas

exposure to air again will allow the desorption of NO_2 molecules, leading to electron re-trapping and subsequent recovery of PL intensity, as demonstrated in time response graph in Fig. 12a, b, c, & d.

Sensing response measurement

The sensing response (S) is the percentage of the ratio of variation of the PL intensity when the sensor is subjected to dry air and a fixed concentration of gas respectively. Equation 9 may be used to calculate it.

$$S\% = \frac{I_g - I_a}{I_g} \times 100, \; I_g > I_a \; and \; S\% = \frac{I_a - I_g}{I_a} \times 100, \; I_a > I_g \quad (9)$$

where I_g denotes the PL intensity of material in presence of NO_2 and I_a represents the PL intensity of material in dry air [38–40]. All the pure and Na-doped ZnO samples, exhibited a rapid response to NO_2 gas, with a low detection limit, as low as 0.5 ppm (500 ppb). The response (S) of all the sensors was enhanced in the high concentration range (0.5–30 ppm), with the exception of pure ZnO, which showed a decrease in response beyond 15 ppm. The substitution of Zn^{2+} with Na^+ introduces additional defects and oxygen vacancies into the ZnO crystal lattice, resulting in a greater concentration of oxygen vacancies in Na-ZnO as compared to ZnO. Consequently, the increased NO_2 adsorption leads to a higher electron concentration, thereby improving the performance of samples with Na doping, as shown in Fig. 10 and systematically detailed in Table 5.

On comparison, it was observed that the pristine ZnO sample exhibited a response (S) of 18.4% in 15 ppm NO_2. In contrast, the samples $ZnO:N_{0.1\%}$, $ZnO:N_{0.2\%}$ and $ZnO:N_{0.3\%}$ exhibited 28.69%, 84.7%, 18.24% response (S) at 25 ppm, 3 ppm and 30 ppm of NO_2 gas respectively, as shown in Fig. 11. The highest response values measured for the each NO_2 concentration are highlighted in the respective graphs. Beyond the concentration of 0.2% of Na, sensitivity declines as the participating electrons increases. The intensity was measured as the average PL integral values obtained after the stabilization in air or NO_2 respectively. It was observed that the samples with smaller nanoparticles and a higher surface-to-volume ratio exhibit higher responses. Also the bare absence of –OH in $ZnO:Na_{0.2\%}$ played an important role in adsorption of NO_2, as it flooded the electrons on the surfaces.

Time response

Figure 12a, b, c and d shows the time response curve between PL emission and time during the sensing measurements, for the samples under the Xenon light radiation at room temperature. The entire set of sensors responded immediately when NO_2 gas was introduced in the test chamber. Each time the concentration of NO_2 inserted was the same amount (ppm) at which the maximum response was observed for the respective sample. When NO_2 was added to the chamber, the PL integrated intensity dropped sharply, indicating its n-type semiconducting nature and stabilizing at a relatively low value. When dry air was supplied again, the integral partially restored its initial value and in turn revealed the excellent recovery characteristics of the sensor. The recovery time (τ_{rec}) represents the time required by the response factor to return to 10% below its equilibrium value

Fig. 12 Time Response Curve of **a** Pure ZnO **b** ZnO:Na$_{0.1\%}$, **c** ZnO:Na$_{0.2\%}$, **d** ZnO:Na$_{0.3\%}$ recorded through Photoluminescence Intensity up to 240 s for 15 ppm, 25 ppm, 30 ppm concentrations of NO$_2$ respectively
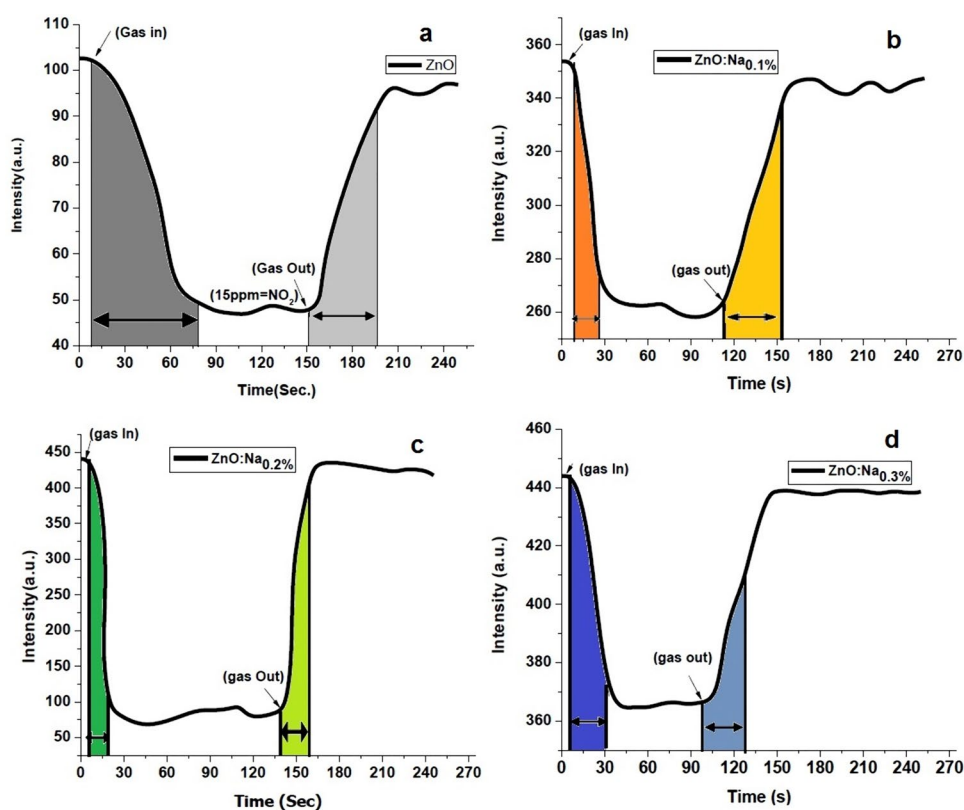
Table 5 Comparative study of response %, response time and recovery time of p-ZnO and of other concentrations of Na-ZnO

Sample	Sensing response (%)	NO$_2$ concentration (ppm)	Response time (Sec)	Recovery time (Sec)
ZnO	18.4	15	74	44
ZnO:N$_{0.1\%}$	28.69	25	17.5	30
ZnO:Na$_{0.2\%}$	84.7	30	09	20
ZnO:Na$_{0.3\%}$	18.24	30	24	29

in air, following a step increase in test gas concentration, whereas the response time or rise time (τ_{res}) represents the time required by the response factor to undergo 90% variation with respect to its equilibrium value following a step increase in the test gas concentration [14, 37, 40–42].

The response and recovery time is lowest in 0.2% Na doped ZnO sample as compared to all other pure and Na doped samples. According to the Kroger VinK Effect [43], these improved sensing properties are attributed to a high surface-to-volume ratio, the hoping effect, and a rise in the density of oxygen vacancies. Introducing the Na atoms into the ZnO lattice, the reaction time was reduced from 1-min 44 s to 13 s and the recovery time decreased from 44 to 20 s. The decrease in response time may be due to two causes; primarily, decreased particle size has larger surface area with increased pore size of sample and secondarily the

large availability of vacant sites or oxygen vacancies on the surface of Na$^+$ for gas adsorption. This response time finally tested at higher concentrations of NO$_2$ gas like (30 ppm). The details recorded may prove to be a great advancement over chemo-resistive sensors [44].

At low level concentration of Sodium in the synthesized systems, it serves as an electron donor which increases the number of free electrons available for interaction with gas, consequently enhancing the sensing response. On contrast, at higher concentrations of Na, it intervenes with the surface matrix, modifying the topography and imperfections which results as a disadvantage in the process of gas adsorption or desorption, compromising the sensing response, response time and recovery time.

Conclusion

The structural characterization of the samples explored by XRD, confirmed the formation of pure ZnO phase. Aqueous solution growth technique seems to be an efficient, inexpensive and easy method used for synthesis of pure and Na$^+$ doped ZnO nanoparticles. Increasing the sodium concentration from (0 to 0.3% w/w) results in peak broadening with a gradual reduction in average crystallite size from 23.95 nm to 18.44 nm, which is due to the

inclusion of strain and indicates the successful amalgamation of Na^+ in ZnO. Na^+ doping in ZnO increased the band gap from 3.03 to 3.08 eV attributed to the larger size of Na^+ cation. Morphology and Selected-area electron diffraction pattern were obtained from SEM and TEM. The ring patterns observed in TEM studies concludes that, the prepared samples were polycrystalline in nature and correlates well with the XRD results. Elemental analysis is carried out using EDS and it is confirmed that only Zinc and oxygen are present in the sample and no other impurities are traced. Increase in the BET Surface and BJH pore size was observed with increasing content of Na. In gas sensing studies, both p-ZnO and ZnO:Na appear to have the best efficiency for NO_2 sensing at room temperature, eliminating the issues associated with heating. The feature observed from Fig. 12a and Fig. 9a, for p-ZnO shows that the PL intensity simultaneously goes down with increasing gas concentration from 500 ppb and show lowest intensity for 15 ppm of NO_2 concentration. On further increasing the NO_2 concentration from 15 ppm, the PL intensity is expected to decrease however, an opposite behavior is observed from the graphs. It is explained on the basis that the 15 ppm NO_2 concentration is high enough to almost saturate the available sites for molecule adsorption, for ZnO:$N_{0.1\%}$, it appears to be 25 ppm and for ZnO:$N_{0.2\%}$ and ZnO:$N_{0.3\%}$ it requires 30 ppm NO_2 to saturate the sites. NO_2 adsorption is almost fully reversible for all the samples as seen by BET analysis, which is confirming the sample recovery. The response of samples was increased for zero to 0.2% Na concentration and then the response starts decreasing when increment in the doping level of Na is introduced as compared to p-ZnO. The highest response of 84.7% is observed for 0.2% Na doped ZnO and the same sample responded in the fastest way to detect the NO_2 gas with 13 s response and 20 s recovery time at room temperature and in its vicinity. Altering the material's optical properties potentially enhances the photoluminescence or light absorption properties, surface area, and interaction with the gas molecules, conclusively sodium (Na) doping in (semiconductor oxides) ZnO can improve gas sensing properties. Also, the PL Sensing is found to be non-destructive fast mechanism and effective method in comparison to methods in solid-state conductometric gas sensors. The study opens a new horizon in the making of novel glow sensors for various gases.

References:

1. W. Jun, W. Zhang, R. Cao, X. You, H. Lai, Analysis of nitrogen dioxide in environment. Adv. Biosci. Biotechnol. **7**(6), 278 (2016)
2. A. Sharma, M. Tomar, V. Gupta, A low temperature operated NO_2 gas sensor based on TeO_2/SnO_2 p–n heterointerface. Sens. Actuators, B Chem. **176**, 875–883 (2013)
3. S. Cui, P. Haihui, S.A. Wells, Z. Wen, S. Mao, J. Chang, M.C. Hersam, J. Chen, Ultrahigh sensitivity and layer-dependent sensing performance of phosphorene-based gas sensors. Nat. Commun. **6**(1), 1–9 (2015)
4. Z. Yin, X. Wang, F. Sun, X. Tong, C. Zhu, Q. Lv, D. Ye, S. Wang, W. Luo, Y.A. Huang, Aligned hierarchical Ag/ZnO nano-heterostructure arrays via electrohydrodynamic nanowire template for enhanced gas-sensing properties. Sci. Rep. **7**(1), 1–10 (2017)
5. Z.L. Wang, Novel nanostructures of ZnO for nanoscale photonics, optoelectronics, piezoelectricity, and sensing. Appl. Phys. A **88**(1), 7–15 (2007)
6. X.-G. Han, H.-Z. He, Q. Kuang, X. Zhou, X.-H. Zhang, T. Xu, Z.-X. Xie, L.S. Zheng, Controlling morphologies and tuning the related properties of nano/microstructured ZnO crystallites. J. Phys. Chem. C **113**(2), 584–589 (2009)
7. M.-W. Ahn, K.-S. Park, J.-H. Heo, J.-G. Park, D.-W. Kim, K.J. Choi, J.-H. Lee, S.-H. Hong, Gas sensing properties of defect-controlled ZnO-nanowire gas sensor. Appl. Phys. Lett. **93**(26), 263103 (2008)
8. N. Han, P. Hu, A. Zuo, D. Zhang, Y. Tian, Y. Chen, Photoluminescence investigation on the gas sensing property of ZnO nanorods prepared by plasma-enhanced CVD method. Sens. Actuators, B Chem. **145**(1), 114–119 (2010)
9. P.A. Murade, V.S. Sangawar, G.N. Chaudhari, V.D. Kapse, A.U. Bajpeyee, Gas sensing performance of nanocrystalline ZnO prepared by a simple route. Mater. Sci.-Pol. **31**(3), 298–305 (2013)
10. W.L. Ong, C. Zhang, G.W. Ho, Ammonia plasma modification towards a rapid and low temperature approach for tuning electrical conductivity of ZnO nanowires on flexible substrates. Nanoscale **3**(10), 4206–4214 (2011)
11. H.B. Lee, M.H.H. Jumali, R.T. Ginting, S.T. Tan, C.C. Yap, C.H. Tan, Mechanistic study on highly crystalline (002) plane bounded ZnO nanofilms prepared via direct current magnetron sputtering. Mater. Lett. **161**, 83–88 (2015)
12. Y. Liu, G. Li, R. Mi, C. Deng, P. Gao, An environment-benign method for the synthesis of p-NiO/n-ZnO heterostructure with excellent performance for gas sensing and photocatalysis. Sens. Actuators, B Chem. **191**, 537–544 (2014)
13. P. Mitra, A.P. Chatterjee, H.S. Maiti, ZnO thin film sensor. Mater. Lett. **35**(1–2), 33–38 (1998)
14. M.K. Mishra, N. Singh, V. Pandey, F.Z. Haque, Synthesis of SnO_2 nanoparticles and its application in sensing ammonia gas through photoluminescence. J. Adv. Phys. **5**(1), 8–12 (2016)
15. M. Madel, J. Jakob, F. Huber, B. Neuschl, S. Bauer, Y. Xie, I. Tischer, K. Thonke, Optical gas sensing by micro-photoluminescence on multiple and single ZnO nanowires. Phys. Status Solidi **212**(8), 1810–1816 (2015)
16. V.V. Gafiychuk, B.K. Ostafiychuk, D.I. Popovych, I.D. Popovych, A.S. Serednytski, ZnO nanoparticles produced by reactive laser ablation. Appl. Surf. Sci. **257**(20), 8396–8401 (2011)
17. V.M. Zhyrovetsky, D.I. Popovych, S.S. Savka, A.S. Serednytski, Nanopowder metal oxide for photoluminescent gas sensing. Nanoscale Res. Lett. **12**(1), 1–5 (2017)
18. B.K. Kotlyarchuk, I.F. Myronyuk, D.I. Popovych, A.S. Serednytski, Synthesis of oxide nanopowder materials and research of their luminescent properties. Phys. Chem. Solid State **7**(3), 490–494 (2006)

19. E. Comini, C. Baratto, G. Faglia, M. Ferroni, G. Sberveglieri, Single crystal ZnO nanowires as optical and conductometric chemical sensor. J. Phys. D Appl. Phys. **40**(23), 7255 (2007)

20. A. Setaro, A. Bismuto, S. Lettieri, P. Maddalena, E. Comini, S. Bianchi, C. Baratto, G. Sberveglieri, Optical sensing of NO_2 in tin oxide nanowires at sub-ppm level. Sens. Actuators, B Chem. **130**(1), 391–395 (2008)

21. N. Singh, A. Umar, N. Singh, H. Fouad, O.Y. Alothman, F.Z. Haque, Highly sensitive ammonia gas sensor based on Sn. J. Power. Sources **294**, 1–7 (2015)

22. N. Singh, A. Umar, N. Singh, H. Fouad, O.Y. Alothman, F.Z. Haque, Highly sensitive optical ammonia gas sensor based on Sn Doped V_2O_5 Nanoparticles. Mater. Res. Bull. **108**, 266–274 (2018)

23. M.R. Parra, F.Z. Haque, Poly (Ethylene Glycol) (PEG)-assisted shape-controlled synthesis of one-dimensional ZnO nanorods. Optik **126**(18), 1562–1566 (2015)

24. Z. Qiu, X. Yang, J. Han, P. Zhang, B. Cao, Z. Dai, G. Duan, W. Cai, Sodium-doped ZnO nanowires grown by high-pressure PLD and their acceptor-related optical properties. J. Am. Ceram. Soc. **97**(7), 2177–2184 (2014)

25. M.R. Parra, F.Z. Haque, Aqueous chemical route synthesis and the effect of calcination temperature on the structural and optical properties of ZnO nanoparticles. J. Market. Res. **3**(4), 363–369 (2014)

26. T.C. Damen, S.P.S. Porto, B. Tell, Raman effect in zinc oxide. Phys. Rev. **142**(2), 570 (1966)

27. J.D. Ye, S.L. Gu, S.M. Zhu, S.M. Liu, Y.D. Zheng, R. Zhang, Y. Shi, Q. Chen, H.Q. Yu, Y.D. Ye, Raman study of lattice dynamic behaviors in phosphorus-doped ZnO films. Appl. Phys. Lett. **88**(10), 101905 (2006)

28. W.W. Li, Z.G. Hu, J.D. Wu, J. Sun, M. Zhu, Z.Q. Zhu, J.H. Chu, Concentration dependence of optical properties in arsenic-doped ZnO nanocrystalline films grown on silicon (100) substrates by pulsed laser deposition. J. Phys. Chem. C **113**(42), 18347–18352 (2009)

29. S. Ameen, V. Ali, M. Zulfequar, M.M. Haq, M. Husain, Photoluminescence, FTIR, and electrical characterization of samarium (III) chloride-doped polyaniline. J. Appl. Polym. Sci. **112**(4), 2315–2319 (2009)

30. M.R. Parra, F. Haque, Optical investigation of various morphologies of ZnO nanostructures prepared by PVP-assisted wet chemical method. Opt. Spectrosc. **118**, 765–772 (2015)

31. Y.-S. Kim, W.-P. Tai, S.-J. Shu, Effect of preheating temperature on structural and optical properties of ZnO thin films by sol–gel process. Thin Solid Films **491**(1–2), 153–160 (2005)

32. R. Mahendran, M. Kashif, T.S. Kumar, M. Saroja, M. Venkatachalam, A. Ayeshamariam, Characterization of manganese doped ZnO (MZO) thin films by spin coating technique. IOSR J. Appl. Phys. **4**(3), 62–68 (2013)

33. V. Pandey, N. Singh, M.M. Malik, F.Z. Khan, SnO_2, SnO_2: Mg and SnO_2: Ni nanoparticles-based luminescence ammonia sensors. Mater. Focus **6**(3), 359–363 (2017)

34. F.Z. Haque, N. Singh, P. Pandey, M.R. Parra, Study of zinc oxide nano/micro rods grown on ITO and glass substrates. Optik **124**(20), 4167–4171 (2013)

35. L. Zhang, Y.Y.H. Guo, G. Liu, Q. Tan, Na-doped ZnO and RGO composite-based flexible acetone gas sensor operated in room temperature. IEEE Access **8**, 171568–171574 (2020)

36. F. Rigoni, C. Pintossi, G. Drera, S. Pagliara, G. Lanti, P. Castrucci, M. De Crescenzi, L. Sangaletti, A cross-functional nanostructured platform based on carbon nanotube-Si hybrid junctions: where photon harvesting meets gas sensing. Sci. Rep. **7**(1), 1–12 (2017)

37. K. Mishra, S. Sheo, R.K. Srivastava, A.C. Panday, S.G. Prakash, Photoluminescence and ultraviolet photoresponse in ZnO nanophorsphors prepared by thermal decomposition of zinc acetate. Adv. Mater. Lett. **2**(4), 298–302 (2011)

38. V. Pandey, "Synthesis and application of metal doped SnO_2 nanostructures in Photoluminescence based NH_3 gas", M.A.N.I.T., India (PhD Thesis) June 2017.

39. D. Valerini, A. Cretì, A.P. Caricato, M. Lomascolo, R. Rella, M. Martino, Optical gas sensing through nanostructured ZnO films with different morphologies. Sens. Actuators, B Chem. **145**(1), 167–173 (2010)

40. N. Singh, F. Syed, F.Z. Haque, Ionic liquid-controlled growth of zinc oxide nano particles and their fluorescence study in the presence of NH_3 gas. Mater. Sci. Res. India **11**(1), 27–34 (2014)

41. N. Singh, V. Pandey, N. Singh, M.M. Malik, F.Z. Haque, Application of TiO_2/SnO_2 nanoparticles in photoluminescence based fast ammonia gas sensing. J. Opt. **46**(3), 199–203 (2017)

42. B.R. Varju, S.A. Wollschlaeger, D.B. Leznoff, Zinc tetracyanoplatinate: a reversible luminescence-based ammonia sensor. Chem.—A Eur. J. **25**(38), 9017–9025 (2019)

43. F.A. Kröger, H.J. Vink, The origin of the fluorescence in self-activated ZnS, CdS, and ZnO. J. Chem. Phys. **22**(2), 250–252 (1954)

44. J. Zhang, D. Zeng, S. Zhao, J. Wu, K. Xu, Q. Zhu, G. Zhang, C. Xie, Room temperature NO_2 sensing: what advantage does the rGO–NiO nanocomposite have over pristine NiO? Phys. Chem. Chem. Phys. **17**(22), 14903–14911 (2015)

45. F. Z. Khan, Sample Holder for Optical Gas Sensing, Patent No.: 373922, Indian Patent, August 2021

46. N.K. Singh, V. Koutu, M.M. Malik, Enhancement of room temperature ferromagnetic behavior of Co-doped ZnO nanoparticles synthesized via sol–gel technique. J. Sol-Gel Sci. Technol. **91**, 324–334 (2019)